

Exciton Dynamics and Quantum Efficiencies in Optically Coupled OLEDs: A Unified Quantum Master Equation Approach

O. Siltanen,^{1,*} K. Luoma,² and K. S. Daskalakis¹

¹*Department of Mechanical and Materials Engineering, University of Turku, Turku, Finland.*

²*Department of Physics and Astronomy, University of Turku, Turku, Finland.*

(Dated: January 6, 2025)

The primary function of organic light-emitting diodes (OLEDs) is to convert electrons into photons. However, only 25 % of the electronic states (singlets) in electrically excited fluorescent molecules can emit light, which is why triplet harvesting has attracted significant attention. Specifically, one often aims to maximize the rate of triplet-to-singlet conversion, while at the same time, it is crucial to depopulate the singlets fast enough—before they convert to triplets or interact with other excited states, potentially breaking molecular bonds. Planar microcavities provide a viable architecture to address these issues. By confining the emitters within planar microcavities one can couple the excitons to cavity modes and engineer the population dynamics to one’s liking. While the weak-coupling regime is renowned for Purcell-enhanced emission, strongly coupled excitons and photons hybridize to form entirely new energy eigenstates known as polaritons. To fully understand and optimize exciton-photon interactions and light-emission mechanisms across various coupling regimes, a unified theory of optically coupled (and uncoupled) OLEDs is needed. In this article, we introduce a quantum master equation model spanning the zero-, weak-, and strong-coupling regimes. We derive the different rates using Fermi’s golden rule and Marcus theory, show how the different regimes converge, and finally evaluate the internal quantum efficiencies in all cases.

I. INTRODUCTION

Organic light-emitting diodes (OLEDs) are revolutionizing display and lighting applications with their unique advantages over traditional inorganic LEDs. Producing vibrant colors, achieving high-contrast ratios, and operating on flexible substrates, OLEDs have become the cornerstone of next-generation devices such as foldable smartphones, advanced televisions, and even transparent displays [1–7]. In addition, it can be eco-friendlier to manufacture and recycle OLEDs than LEDs [8–11]. Despite of their benefits, there are some inherent challenges with OLEDs that have hindered their adoption in a wider range of applications, particularly in general illumination. Most notably, excitons can exist in two fundamentally different spin configurations: one singlet state and three triplet states [12].

The singlet exciton is the only one that can efficiently and rapidly emit light through fluorescence. In contrast, triplet excitons cannot directly emit photons due to spin conservation rules, making them non-emissive in typical fluorescent OLEDs [3]. The non-emitting triplet states not only fail to contribute to light output but also pose additional challenges. At higher input currents and exciton densities, triplet excitons are more likely to interact with other excitons or polarons. These interactions convert excitonic energy into heat rather than light, reducing the overall efficiency of the device—a phenomenon known as efficiency roll-off [13–15]. Furthermore, the accumulation of long-lived triplet states increases the likelihood of collisions that can break molecular bonds, causing irreversible degradation of the organic materials [16].

The issues outlined above can be addressed using planar microcavity architectures [17–21]. By embedding the emitting molecules within optical cavities and engineering the photonic environment, it becomes possible to control exciton dynamics and enhance light emission. In the weak-coupling regime, the Purcell effect increases the radiative decay rate of singlet excitons, thereby improving overall emission efficiency [22]. Furthermore, as the singlets depopulate quickly enough, they do not have time to convert into harmful triplets via inter-system crossing (ISC). For phosphorescent OLEDs, this is equivalent to Purcell-suppressed reverse ISC (RISC) [19]. In this article, OLEDs operating in the weak-coupling regime are referred to as microcavity OLEDs (MOLEDs).

In the strong-coupling regime, where exciton-photon interactions exceed exciton-photon losses, light and matter hybridize to form collective energy eigenstates known as (exciton) polaritons [23–27]. Polaritons offer new opportunities to manipulate energy transfer processes. For instance, in the few-molecule case, where the number of coupled emitters is sufficient to preserve polaritonic effects, RISC can be enhanced by tuning the lower polariton below the first-order triplet state [28–31]. We call OLEDs in this regime polariton OLEDs (POLEDs). Fig. 1(a) shows a single molecule in such a device.

While both coupling regimes provide unique advantages, fully understanding and exploiting the exciton-photon interactions remains a challenging yet promising frontier in OLED optimization. Theoretical insights in this regard often rely on quantum master equations [32–38]. Despite recent advancements, a comprehensive master equation model covering all the coupling regimes has been missing. Such a unified model could bridge the gap between different coupling regimes and provide a more complete understanding of light-emission mechanisms in

* olmisi@utu.fi

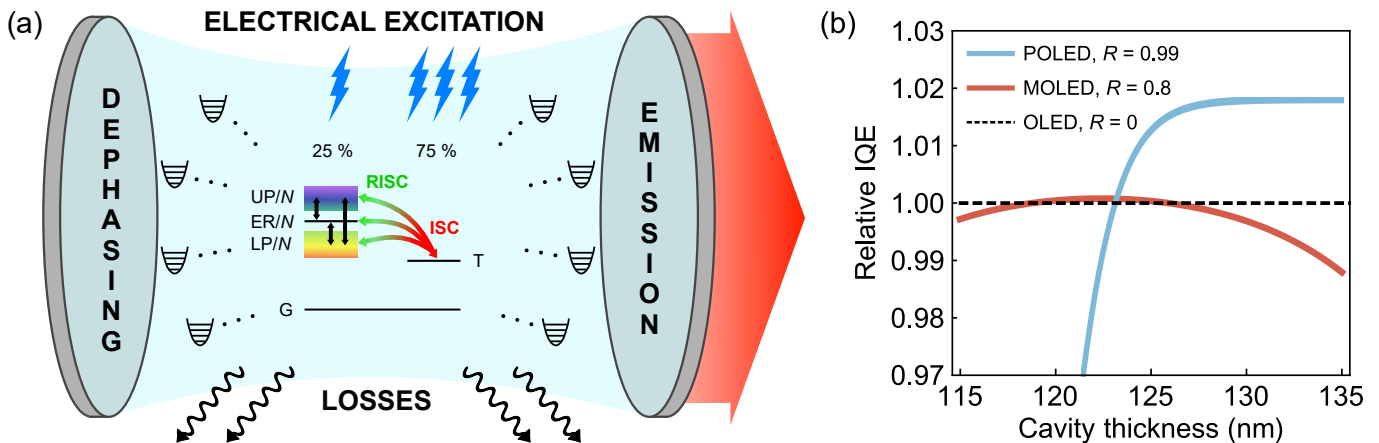


FIG. 1. (a) A schematic picture of the system: organic molecule(s) inside an optical cavity. We consider no coupling (OLEDs), weak coupling (MOLEDs), and strong coupling with the cavity mode (POLEDs). The molecules are weakly coupled to the surrounding phonon bath and experience electrical excitation, polariton transitions, dephasing, ISC, RISC, emission, and nonradiative losses. Even though a single, strongly coupled molecule with its polariton contributions is shown, we consider an ensemble of N molecules. UP/N = one N th of upper polariton [cf. Eq. (14)], ER/N = one N th of exciton reservoir, LP/N = one N th of lower polariton, T = triplet, G = ground state. (b) A snapshot of the main results: (relative) internal quantum efficiencies (IQEs) of OLEDs ($R = 0$), MOLEDs ($R = 0.8$), and POLEDs ($R = 0.99$) as functions of cavity thickness, normalized to OLED IQE. R = mirror reflectivity and $N = 10^6$. Other parameters are given in Table I.

these devices, guiding the design of more efficient OLEDs. In this article, we take the first steps in developing such a model.

Starting from the Holstein-Tavis-Cummings (HTC) Hamiltonian [34, 35], and using both the Fermi's golden rule (FGR) [39] and Marcus theory of electron transfer [40], we derive rates for electrical excitation, polariton transitions, dephasing, ISC, RISC, emission, and nonradiative losses, as schematically illustrated in Fig. 1(a). Then, using the Gorini-Kossakowski-Sudarshan-Lindblad (GKSL) master equation of open quantum systems [41], we solve the system's population dynamics in all the coupling regimes. We apply our model in estimating the system's internal quantum efficiency (IQE), i.e., the ratio of photons generated to excitons formed by injected charge carriers. Fig. 1(b) shows a snapshot of these results. With optimized cavity parameters, our model predicts the cavity advantage of approximately 2% for 1,3,5-tris(4-(diphenylamino)phenyl)-2,4,6-tricyanobenzene (3DPA3CN). Even though we restrict ourselves to weakly coupled environment and linear processes, we believe our results will help with actual device design, particularly in optimizing the cavity thickness and mirror reflectivity.

This article is structured as follows. In Sec. II, we present a detailed description of our model, focusing on the derivation and comparison of all the different POLED rates. As we shall see, the majority of MOLED and OLED rates can be expressed in terms of these rates. In Sec. III, we demonstrate how the classical rate equations emerge from the model and how they change, as we first approach the MOLED case and eventually the basic OLED case with decreasing light-matter coupling strength (or increasing cavity losses). In Sec. IV, we use

the steady-state solutions of these rate equations to evaluate the IQE in all the coupling regimes. Finally, Sec. V provides a summary, conclusions, and discussion.

II. THEORY

A. Hamiltonian and main assumptions

Our system of interest consists of N identical organic molecules coupled to a single cavity mode. We consider

TABLE I. Example parameters used in this article.

Parameter	Value
N	10^6
V_{st}	20 μeV
λ_{st}	100 meV
λ_{gt}	330 meV
μ	9×10^{-30} Cs
E_s	2.51 eV
E_t	2.41 eV
$E_{s,cut}$	80 meV
$E_{t,cut}$	70 meV
n_{eff}	2
$\gamma(J)$	1
J	100 mA/cm ²
A	1 μm^2
T	293 K
R	0.99

the weak-pumping and weak system-environment coupling regimes. That is, the molecules are assumed to carry at most one exciton at a time, and the exciton is weakly coupled to the surrounding phonon bath, which we assume is common for all the molecular sites. Taking both the singlets (S) and triplets (T) into account, we can describe the system with the HTC Hamiltonian $H = H_S + H_B + H_I$ [34, 35]. Using the rotating-wave approximation and omitting the triplet-cavity mode couplings, we have

$$H_S = \sum_{n=1}^N E_s |S_n\rangle\langle S_n| + \sum_{n=1}^N E_t |T_n\rangle\langle T_n| + E_c \hat{a}^\dagger \hat{a} + V_{st} \sum_{n=1}^N (|S_n\rangle\langle T_n| + |T_n\rangle\langle S_n|) + g_1 \sum_{n=1}^N (|S_n\rangle\langle \mathcal{G}| \hat{a} + |\mathcal{G}\rangle\langle S_n| \hat{a}^\dagger), \quad (1)$$

$$H_B = \sum_l \epsilon_l \hat{b}_l^\dagger \hat{b}_l, \quad (2)$$

$$H_I = \hbar \sum_l \sum_{n=1}^N (\sigma_l |S_n\rangle\langle S_n| + \tau_l |T_n\rangle\langle T_n|) (\hat{b}_l + \hat{b}_l^\dagger). \quad (3)$$

Here, E_s and E_t are the $^*0 \leftrightarrow 0$ transition energies. This simplification makes it more straightforward and meaningful to compare the different coupling regimes. Namely, while it is typically the $^*0 \rightarrow 2$ ($0 \rightarrow 2^*$) transition that dominates weak (strong) coupling, focusing on the $^*0 \leftrightarrow 0$ transition allows us to consider both simultaneously within a unified framework. Physically, this would mean internal conversion being faster than any other timescale in the system, effectively redistributing population to the lowest vibrational state before any significant emission or absorption event occurs.

\hat{a}^\dagger (\hat{a}) is the creation (annihilation) operator of a photon with the energy E_c . For simplicity, we restrict our attention to the smallest possible energy $E_c = \pi \hbar c / (n_{\text{eff}} L_c)$, where n_{eff} and L_c are the cavity's refractive index and thickness, respectively. V_{st} is the singlet-triplet coupling strength. Global ground state is denoted by $|\mathcal{G}\rangle$. $g_N = \mu \sqrt{N E_c} / (2 \epsilon_0 V)$ is the light-matter coupling strength with μ and V being the transition dipole moment (TDM) and mode volume, respectively. The TDM of triplets is typically negligible [23], which allowed us to omit the triplet-cavity mode interactions. \hat{b}_l^\dagger (\hat{b}_l) is the creation (annihilation) operator of a delocalized phonon with the energy ϵ_l . Finally, σ_l (τ_l) is the coupling strength between the l th harmonic mode and a singlet (triplet) exciton. While more realistic models would consider a continuum of cavity modes [42], direct sums of H often give sufficient fits in multimode experiments [43].

Since one of our objectives is to assist with actual device design, the effects of cavity thickness should be taken more accurately into account; By tuning L_c , one can adjust E_c out of resonance with E_s , in which case the coupling strength should gradually vanish. However, this

does not occur with the current definition of g_N .

Writing H_S in the interaction picture and performing time coarse graining over some adequate timescale Δt [44], we get

$$H'_S \approx \frac{g_1}{\Delta t} \sum_{n=1}^N \int_0^{\Delta t} \left(e^{i(E_s - E_c)s/\hbar} |S_n\rangle\langle \mathcal{G}| \hat{a} + e^{-i(E_s - E_c)s/\hbar} |\mathcal{G}\rangle\langle S_n| \hat{a}^\dagger \right) ds. \quad (4)$$

Assuming small disorder in the singlet energies, the detunings become independent. And because $N \gg 0$, central limit theorem allows us to replace the uniform distributions with Gaussians. Evaluating the integrals and returning to the Schrödinger picture, we can replace g_N with

$$g_{\text{eff}} \approx g_N e^{-\frac{1}{2} \left(\frac{E_s - E_c}{E_{\text{cut}}} \right)^2}. \quad (5)$$

Here, E_{cut} is a cut-off energy that should satisfy $E_{\text{cut}} \gg g_1$ for the interaction-picture state to remain nearly constant over the averaging interval Δt [45]. Accordingly, we use $E_{\text{cut}} = g_1 \times 10^4$. While the detailed derivation of optimal E_{cut} falls outside the scope of this article, this specific value—with the rest of the parameters—will allow a tuning range of ± 20 nm for the cavity thickness, which is consistent with prior works (see, e.g., Refs. [19, 24]). In actual experiments, E_{cut} could be treated as a fitting parameter. In fact, Eq. (5) has been shown to provide good experimental fits in similar physical systems [46, 47].

Let us proceed by diagonalizing the system Hamiltonian. Assuming the dominance of light-matter coupling and that $V_{st} \ll |E_s - E_t|$, $\hbar \sigma_l \ll |E_s - \epsilon_l|$, $\hbar \tau_l \ll |E_t - \epsilon_l|$, H_S can be diagonalized (nearly) independently from the singlet-triplet couplings and H_I . In the triplet manifold, we get the N trivial eigenstates $|T_n\rangle$. In the polariton manifold, we get the following $N + 1$ eigenstates,

$$|P_+\rangle = \frac{\alpha}{\sqrt{N}} \sum_{n=1}^N |S_n\rangle \otimes |0\rangle + \beta |\mathcal{G}\rangle \otimes |1\rangle, \quad (6)$$

$$|P_-\rangle = \frac{\beta}{\sqrt{N}} \sum_{n=1}^N |S_n\rangle \otimes |0\rangle - \alpha |\mathcal{G}\rangle \otimes |1\rangle, \quad (7)$$

$$|D_k\rangle = \frac{1}{\sqrt{N}} \sum_{n=1}^N e^{i2\pi nk/N} |S_n\rangle \otimes |0\rangle, k \in [1, N - 1]. \quad (8)$$

$|P_+\rangle$ is the upper polariton (UP), $|P_-\rangle$ is the lower polariton (LP), and $|D_k\rangle$ are the dark states, which are collectively referred to as the exciton reservoir (ER). The parameters α and β satisfy

$$|\alpha|^2 = \frac{1}{2} \left(1 + \frac{E_s - E_c}{\sqrt{(E_s - E_c)^2 + 4g_{\text{eff}}^2}} \right), \quad (9)$$

$$|\beta|^2 = \frac{1}{2} \left(1 - \frac{E_s - E_c}{\sqrt{(E_s - E_c)^2 + 4g_{\text{eff}}^2}} \right), \quad (10)$$

the squares being known as the Hopfield coefficients, whereas the eigenenergies of the polaritons are

$$E_{\pm} = \frac{E_s + E_c}{2} \pm \sqrt{g_{\text{eff}}^2 + \frac{(E_s - E_c)^2}{4}}. \quad (11)$$

Note that, due to the omitted phonon couplings, these energies actually correspond to the centers of the polariton spectra. The $N - 1$ dark states, in turn, share the eigenenergy E_s .

B. Gorini-Kossakowski-Sudarshan-Lindblad master equation and jump operators

The time evolution of open quantum systems ρ , caused by inevitable interactions with the environment, is captured by the GKSL master equation [41]

$$\dot{\rho} = -\frac{i}{\hbar}[H_S, \rho] + \sum_k \Gamma_k \left(\hat{L}_k \rho \hat{L}_k^\dagger - \frac{1}{2} \{ \hat{L}_k^\dagger \hat{L}_k, \rho \} \right). \quad (12)$$

The commutator $[H_S, \rho] := H_S \rho - \rho H_S$ gives the unitary dynamics of the system, while the sum over jump operators \hat{L}_k gives the non-unitary, environment-induced dynamics. Each channel is weighted by the rate Γ_k , and the anti-commutator is defined as $\{X, Y\} := XY + YX$.

Eq. (12) is the main tool of this article. That is, ρ describes the joint state of singlets, triplets, and cavity mode. All the processes we are interested in are schematically visualized in Fig. 1(a), and we will derive their rates in the following subsections.

C. Electrical excitation

Let us begin by constructing phenomenological operators for electrical excitation and the corresponding rates. In the singlet-triplet basis, we can consider the simple projections $|S_n\rangle\langle\mathcal{G}|$ and $|T_n\rangle\langle\mathcal{G}|$ with the rates $\Gamma_{\mathcal{G}\rightarrow T_n} = 3\Gamma_{\mathcal{G}\rightarrow S_n}$; For clarity, we omit the specific spin configurations of triplets and only require there to be three times as many triplets as singlets.

From a simplistic point of view, $\Gamma_{\mathcal{G}\rightarrow S_n}$ depends on only two factors: how many electrons and holes per second and molecular site are injected to the system and where the available sites are located. The number of electrons per second is given by the ratio of current and elementary charge, I/e , which we can also write in terms of the current density J and the mode volume's effective cross-section A as JA/e . To account for correct spin configurations and possible electron-hole mismatch, we multiply by $\gamma(J)/4$, where $\gamma(J)$ is the electron-hole balance ratio [48]. Taking the sites into account, we get $\gamma(J)JA/(4eN)$; The more sites there are, the less probable it is for the specific site n to get excited.

Then, say the electrons and holes move at the drift velocities v_e and v_h , respectively, and once they meet

somewhere between the electrodes, they combine to form excitons in the characteristic recombination time $\tau = \Delta z^2/(4D_{\text{eff}})$ [49]. Here, Δz is the width of the exciton formation zone and $D_{\text{eff}} = D_e D_h / (D_e + D_h)$ is the effective diffusion coefficient of electrons and holes. Assuming equal probability for all sites inside the exciton formation zone to get excited and zero outside of it, we get the pumping rate

$$\Gamma_{\mathcal{G}\rightarrow S_n} = \chi \left(\frac{v_e L}{v_e + v_h} - \sqrt{D_{\text{eff}}\tau}, \frac{v_e L}{v_e + v_h} + \sqrt{D_{\text{eff}}\tau}, z_n \right) \times \frac{\gamma(J)JA}{4eN}, \quad (13)$$

where L is the distance between the electrodes, z_n is the distance between the n th molecule and cathode, and $\chi(z_1, z_2, z) = 1$ if $z \in [z_1, z_2]$ and $\chi(z_1, z_2, z) = 0$ otherwise.

Moving to the polariton basis, we get

$$|S_n\rangle = \frac{1}{\sqrt{N}} \left(\alpha^* |P_+\rangle + \beta^* |P_-\rangle + \sum_{k=1}^{N-1} e^{-i\frac{2\pi nk}{N}} |D_k\rangle \right), \quad (14)$$

and the polaritonic pumping rates can be identified as

$$\Gamma_{\mathcal{G}\rightarrow P_+} = |\alpha|^2 \langle \Gamma_{\mathcal{G}\rightarrow S_n} \rangle, \quad (15)$$

$$\Gamma_{\mathcal{G}\rightarrow D_k} = \langle \Gamma_{\mathcal{G}\rightarrow S_n} \rangle, \quad (16)$$

$$\Gamma_{\mathcal{G}\rightarrow P_-} = |\beta|^2 \langle \Gamma_{\mathcal{G}\rightarrow S_n} \rangle, \quad (17)$$

where $\langle \bullet \rangle$ denotes the arithmetic mean over all molecular sites. Here we omitted possible polariton coherences, but that is justified in the presence of very strong dephasing.

D. Polariton transitions and dephasing

Transitions between polaritons (including the dark states) are given by the projections $|f\rangle\langle i|$, where $i, f = P_{\pm}, D_k$ and $i \neq f$. In dephasing, we have $i = f$. We calculate the rates $\Gamma_{i\rightarrow f}$ using FGR [3, 39],

$$\Gamma_{i\rightarrow f} = \frac{2\pi}{\hbar} |\langle f | H_I | i \rangle|^2 / \text{eV}. \quad (18)$$

Note that here we have seemingly omitted the density of states, since we are interested in the transition rates between *pairs* of states and not, e.g., UP and *all* the dark states simultaneously.

1. UP-to-ER and ER-to-UP

The UP-to-ER coupling term can be identified by writing the term $|S_n\rangle\langle S_n|$ in H_I in the polariton basis. Because moving from UP to ER means *creating* a (high-energy) phonon, we can omit the annihilation operators \hat{b}_l . As the final bath state, we use $\hat{b}_l^\dagger \rho_{lh} \hat{b}_l / \text{tr}[\bullet]$

and its purification $|\psi_{th+1}\rangle = \hat{b}_l^\dagger |\psi_{th}\rangle / \sqrt{\text{tr}[\bullet]}$. Here, l' labels the harmonic mode of the transition energy $\Delta_{+s} = E_+ - E_s$. We take multiphonon processes to be negligible. Using the definition of the spectral density $J(E) := 2\pi\hbar \sum_l |\sigma(E_l)|^2 \delta(E - E_l) = 2\pi\hbar |\sigma(E)|^2 / \text{eV}$ [41], we get

$$\Gamma_{P_+ \rightarrow D_k} = \frac{2\pi}{\hbar} \left| \langle D_k | \otimes \langle \psi_{th+1} | \sum_{l,n} \frac{\alpha \hbar \sigma_l}{N} e^{-i \frac{2\pi n k}{N}} | D_k \rangle \right. \\ \left. \langle P_+ | \hat{b}_l^\dagger | P_+ \rangle \otimes |\psi_{th}\rangle \right|^2 / \text{eV} \quad (19)$$

$$= \frac{2\pi\hbar |\alpha|^2}{N^2 \text{tr}[\bullet]} \\ \left| \sum_{l,n} \sigma_l e^{-i \frac{2\pi n k}{N}} \langle \psi_{th} | \hat{b}_l \hat{b}_l^\dagger | \psi_{th} \rangle \right|^2 / \text{eV} \quad (20)$$

$$= \frac{2\pi\hbar |\alpha|^2}{\text{tr}[\bullet]} \\ |\sigma_l|^2 \langle \psi_{th} | (\hat{b}_l \hat{b}_l + \mathbf{1}) | \psi_{th} \rangle^2 / \text{eV} \quad (21)$$

$$= |\alpha|^2 J(\Delta_{+s}) \text{tr}[\bullet] \quad (22)$$

$$= |\alpha|^2 J(\Delta_{+s}) [n(\Delta_{+s}) + 1], \quad (23)$$

where $n(E)$ is the Bose-Einstein distribution,

$$n(E) = \frac{1}{e^{\frac{E}{k_B T}} - 1}. \quad (24)$$

The ER-to-UP transition rate is given by otherwise the same approach but with $\hat{b}_{l,n}$ and $|\psi_{th-1}\rangle$ instead of $\hat{b}_{l,n}^\dagger$ and $|\psi_{th+1}\rangle$. This gives us

$$\Gamma_{D_k \rightarrow P_+} = |\alpha|^2 J(\Delta_{+s}) n(\Delta_{+s}). \quad (25)$$

Throughout the rest of this article, we shall use the super-Ohmic spectral density with the cut-off energy $E_{s,cut}$,

$$J(E) = \frac{1}{\hbar} \frac{E^3}{E_{s,cut}^2} e^{-E/E_{s,cut}}. \quad (26)$$

2. ER-to-LP and LP-to-ER

Here, the FGR calculations yield

$$\Gamma_{D_k \rightarrow P_-} = |\beta|^2 J(\Delta_{s-}) [n(\Delta_{s-}) + 1], \quad (27)$$

$$\Gamma_{P_- \rightarrow D_k} = |\beta|^2 J(\Delta_{s-}) n(\Delta_{s-}). \quad (28)$$

3. UP-to-LP and LP-to-UP

Finally, the transition rates between the bright polaron states become

$$\Gamma_{P_+ \rightarrow P_-} = |\alpha|^2 |\beta|^2 J(\Delta_{+-}) [n(\Delta_{+-}) + 1], \quad (29)$$

$$\Gamma_{P_- \rightarrow P_+} = |\alpha|^2 |\beta|^2 J(\Delta_{+-}) n(\Delta_{+-}). \quad (30)$$

With g_{eff} approaching zero, we can see that the transition rates weighted by $|\beta|^2$ approach zero as well. In the weak-coupling regime, however, the light-matter coupling can be treated as a perturbation, and the rates $\Gamma_{P_+ \rightarrow P_-}$ and $\Gamma_{D_k \rightarrow P_-}$ are replaced by

$$\Gamma_{S_n \rightarrow M}^{weak} = F_P \frac{E_s^3 \mu^2}{3\pi\epsilon_0 \hbar^4 c^3} e^{-\frac{1}{2} \left(\frac{E_s - E_c}{E_{cut}} \right)^2}, \quad (31)$$

where M stands for (cavity) mode and F_P is the Purcell factor [50]

$$F_P = \frac{3}{4\pi^2} \frac{Q}{V} \left(\frac{2\pi\hbar c}{E_s} \right)^3. \quad (32)$$

Here, Q is the cavity quality factor that can be written in terms of the cavity mirrors' reflectivities R as [3]

$$Q = \frac{E_c L_c}{\hbar c} \frac{\sqrt{R}}{1 - R}. \quad (33)$$

As the loss rates dominate in this regime, we can assume that the photon escapes the cavity before it can re-excite the singlets. Hence, we set the upward rates to zero.

4. Dephasing

Because with dephasing there is no energy exchange with the environment, the initial and final bath states are the same (in energy). Therefore $\langle f | H_I | i \rangle = 0$ and we need to apply the second-order perturbation theory [51],

$$\Gamma_{i \rightarrow f} = \frac{2\pi}{\hbar} \sum_m \left| \frac{\langle f | H_I | m \rangle \langle m | H_I | i \rangle}{E_i - E_m} \right|^2 / \text{eV}, \quad m \neq i. \quad (34)$$

Whenever the intermediate bath state $|m\rangle$ is above $|i\rangle = |f\rangle$ in energy (i.e., when the intermediate *system* state is *lower* in energy), we use the intermediate state $|\psi_{th+1}\rangle$. And whenever $|m\rangle$ is lower in energy, we use the intermediate state $|\psi_{th-1}\rangle$.

The dephasing rates for UP, ER, and LP become

$$\Gamma_{P_+} = \frac{\hbar}{2\pi} \left\{ (N-1) \frac{|\alpha|^4}{\Delta_{+s}^2} J(\Delta_{+s})^2 [n(\Delta_{+s}) + 1]^2 \right. \\ \left. + \frac{|\alpha|^4 |\beta|^4}{\Delta_{+-}^2} J(\Delta_{+-})^2 [n(\Delta_{+-}) + 1]^2 \right\} \times \text{eV}, \quad (35)$$

$$\Gamma_{D_k} = \frac{\hbar}{2\pi} \left\{ \frac{|\alpha|^4}{\Delta_{+s}^2} J(\Delta_{+s})^2 n(\Delta_{+s})^2 \right. \\ \left. + \frac{|\beta|^4}{\Delta_{s-}^2} J(\Delta_{s-})^2 [n(\Delta_{s-}) + 1]^2 \right\} \times \text{eV}, \quad (36)$$

$$\Gamma_{P_-} = \frac{\hbar}{2\pi} \left\{ \frac{|\alpha|^4 |\beta|^4}{\Delta_{+-}^2} J(\Delta_{+-})^2 n(\Delta_{+-})^2 \right. \\ \left. + (N-1) \frac{|\beta|^4}{\Delta_{s-}^2} J(\Delta_{s-})^2 n(\Delta_{s-})^2 \right\} \times \text{eV}, \quad (37)$$

respectively. Eq. (36) also gives the transition rate between different dark states, $\Gamma_{D_k \rightarrow D_{k'}} = \Gamma_{D_k}$. However, if the different dark states behave in a symmetric fashion, these transitions cancel out.

E. ISC and RISC

ISC and RISC are important processes from the point of view of triplet harvesting. While the singlet-to-triplet ISC rate should be minimized, the triplet-to-singlet RISC rate should be maximized. According to the celebrated Marcus theory of electron transfer, these rates are given—under the assumption of very fast internal conversion, i.e., when the lowest vibrational levels dominate—by [3, 40]

$$k_M(i, f) = \frac{2\pi}{\hbar} |\langle f | H_{st} | i \rangle|^2 \rho(E_{if}) \quad (38)$$

$$= \frac{V_{st}^2}{\hbar} \sqrt{\frac{\pi}{\lambda_{fi} k_B T}} e^{-\frac{(\lambda_{fi} + \Delta_{fi})^2}{4\lambda_{fi} k_B T}}. \quad (39)$$

Here, H_{st} is the singlet-triplet interaction term appearing in the HTC Hamiltonian, $\rho(E_{if})$ is the joint density of states of the initial and final wavefunctions, $\lambda_{fi} = \lambda_{if}$ is the reorganization energy—independent of the process's direction—and $\Delta_{fi} = E_f - E_i$ is the change of free energy.

1. ISC

Applying Eqs. (38) and (39) to UP, we get the ISC rate

$$\Gamma_{P_+ \rightarrow T_n} = \frac{2\pi}{\hbar} |\langle T_n | H_{st} | P_+ \rangle|^2 \rho(E_{+t}) \quad (40)$$

$$= \frac{2\pi}{\hbar} \left| V_{st} \frac{\alpha}{\sqrt{N}} \right|^2 \rho(E_{+t}) \quad (41)$$

$$= \frac{|\alpha|^2}{N} k_M(+, t). \quad (42)$$

Similar calculations for the dark states and LP yield

$$\Gamma_{D_k \rightarrow T_n} = \frac{1}{N} k_M(s, t), \quad (43)$$

$$\Gamma_{P_- \rightarrow T_n} = \frac{|\beta|^2}{N} k_M(-, t). \quad (44)$$

2. RISC

The RISC rates differ from the corresponding ISC rates only in terms of the order of arguments,

$$\Gamma_{T_n \rightarrow P_+} = \frac{|\alpha|^2}{N} k_M(t, +), \quad (45)$$

$$\Gamma_{T_n \rightarrow D_k} = \frac{1}{N} k_M(t, s), \quad (46)$$

$$\Gamma_{T_n \rightarrow P_-} = \frac{|\beta|^2}{N} k_M(t, -). \quad (47)$$

3. Reorganization energies

In Ref. [29], the authors defined the polaritonic reorganization energies as $(\sqrt{\lambda_{st}} + \sqrt{\lambda_{gt}})^2$, where g stands for the electronic ground state. This definition, however, does not take into account the different excitonic/photon contents of UP and LP. For example, either one can be fully excitonic, in which case the reorganization energy should just be λ_{st} . Hence, we define the polaritonic reorganization energies differently.

The reorganization energy is more generally defined as [3]

$$\lambda_{fi} = \frac{1}{2} \kappa (Q_f - Q_i)^2, \quad (48)$$

where κ is the curvature of the potential energy surfaces (same for initial and final states) and $Q_{i(f)}$ is the nuclear coordinate of the initial (final) state. Assuming that the nuclear coordinate of UP is the convex combination $Q_+ = |\alpha|^2 Q_s + |\beta|^2 Q_g$ and similarly for LP, it is quite straightforward to show that

$$\lambda_{+t} = (|\alpha|^2 \sqrt{\lambda_{st}} + |\beta|^2 \sqrt{\lambda_{gt}})^2, \quad (49)$$

$$\lambda_{-t} = (|\beta|^2 \sqrt{\lambda_{st}} + |\alpha|^2 \sqrt{\lambda_{gt}})^2. \quad (50)$$

F. Emission

Emission from POLEDs and MOLEDs is described by the annihilation operator \hat{a} and the rate [37]

$$\kappa = \frac{E_c}{2Q\hbar}. \quad (51)$$

When $R = 0$, also $Q = 0$ and the photon immediately escapes the “cavity”. In this case—effectively the bare-film case—the rate of emission is actually given by $\Gamma_{S_n \rightarrow M}^{weak}$ with $F_P = 1$ and $E_{cut} = \infty$. We denote this rate by $\Gamma_{S_n \rightarrow M}^{free}$. Setting $E_{cut} = \infty$ is equivalent to the emitter freely emitting to the continuum of available modes without any spectral selectivity or restrictions, which aligns with the scenario of no coupling to a cavity mode.

G. Nonradiative losses

The nonradiative relaxation rates of singlet and triplet excitons can be estimated with FGR. In the polariton manifold, we get

$$\Gamma_{P_+ \rightarrow \mathcal{G}} \approx |\alpha|^2 J(E_+) [n(E_+) + 1], \quad (52)$$

$$\Gamma_{D_k \rightarrow \mathcal{G}} \approx J(E_s) [n(E_s) + 1], \quad (53)$$

$$\Gamma_{P_- \rightarrow \mathcal{G}} \approx |\beta|^2 J(E_-) [n(E_-) + 1]. \quad (54)$$

As for the triplets, we get

$$\Gamma_{T_n \rightarrow \mathcal{G}} \approx \tilde{J}(E_t) [n(E_t) + 1]. \quad (55)$$

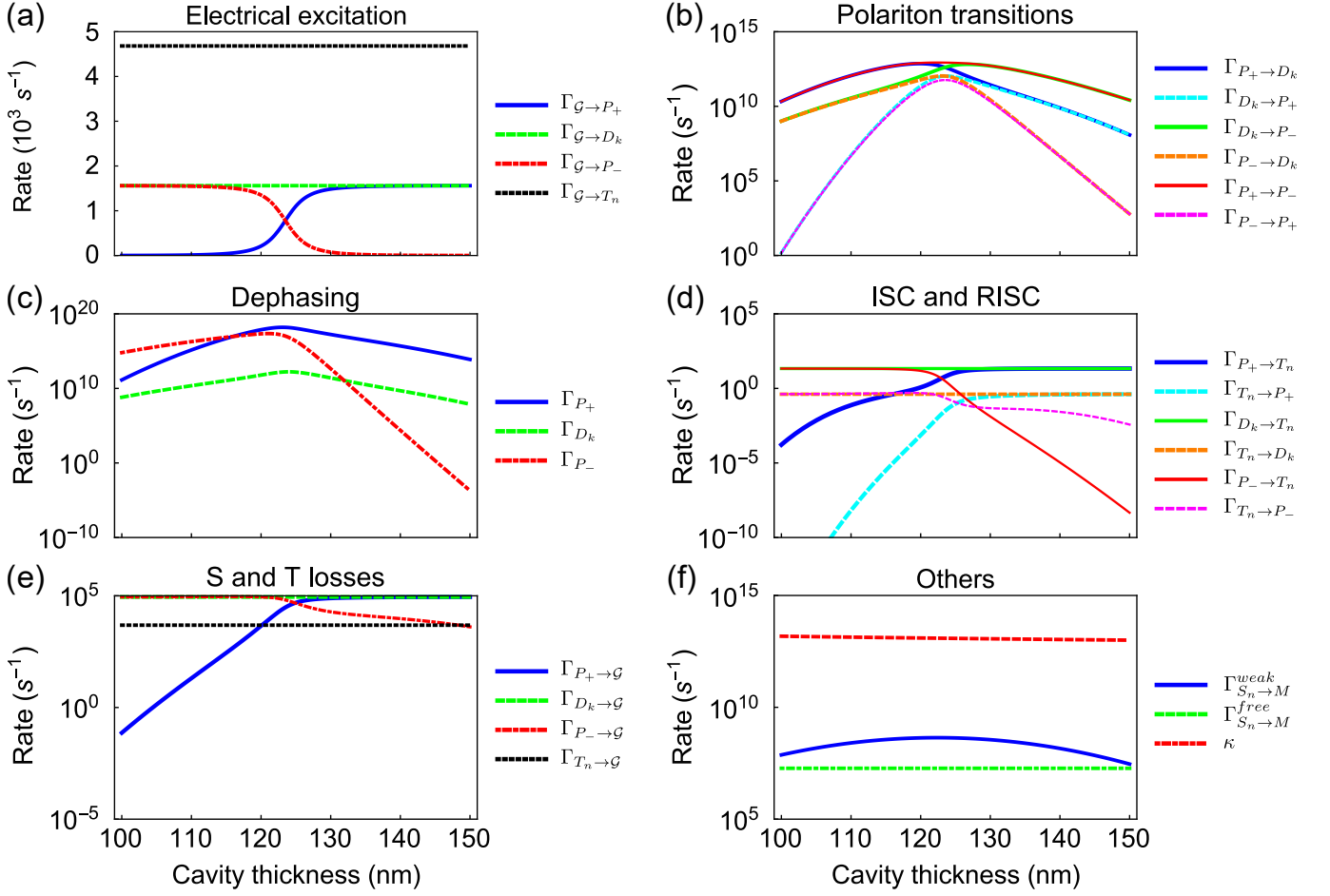


FIG. 2. Rates of linear processes in optically coupled OLEDs at normal incidence, as functions of the cavity thickness. Note the logarithmic scale in all the other panels except (a).

The spectral density $\tilde{J}(E)$ of triplets may differ from $J(E)$ in terms of its cut-off energy.

$\Gamma_{D_k \rightarrow G}$ can be used to evaluate whether we are in the strong-coupling regime, which occurs if [23, 52]

$$\frac{\hbar(\Gamma_{D_k \rightarrow G} + \kappa)}{2} < 2g_{\text{eff}} < \frac{\min\{E_s, E_c\}}{5}. \quad (56)$$

With smaller coupling strengths we are in the weak-coupling regime, i.e., we are dealing with either MOLEDs or basic OLEDs. With larger coupling strengths, we enter the ultrastrong-coupling regime, where the rotating-wave approximation does not hold anymore.

H. Comparative overview

The cavity thickness L_c —modulating the cavity photon's energy E_c —clearly has a significant impact on nearly all the rates derived above, as shown in Fig. 2. We use 3DPA3CN as an example molecule due to it being well-characterized in the existing literature [29, 53]. The material-specific parameters are listed in Table I, along

with other example parameters used in this article. We calculate the mode volume using [54]

$$V = \frac{\int \epsilon \langle \hat{E}^2 \rangle d^3 \mathbf{r}}{\max\{\epsilon \langle \hat{E}^2 \rangle\}}, \quad (57)$$

where ϵ is the dielectric function and $\hat{E} = \sqrt{E_c/(\epsilon_0 V)}(\hat{a} + \hat{a}^\dagger) \sin(qz)$, with wave number q and position z , is the electric-field operator inside the cavity [55]. Assuming constant ϵ , or absorbing any of its spatial variations into the average cross-section A , we find $V = AL_c/2$. For simplicity, we further assume that all the molecular sites lie within the exciton formation zone.

With our parameter choices, the singlet and cavity mode are in resonance at $L_c \approx 123$ nm. This is especially evident from Fig. 2(a), where the rates of electrically exciting UP and LP are not only equal but symmetric around this point. In fact, the LP and UP pumping rates are essentially just the Hopfield coefficients; The more excitonic they are, the more closely they follow the pumping rate of the entirely excitonic ER. This applies for the transition rates in Fig. 2(b), (R)ISC rates

in Fig. 2(d), and nonradiative rates in Fig. 2(e) too. Importantly, for large N , electrical excitation is governed almost exclusively by the ER and triplet manifold.

Even though the downward transitions in Fig. 2(b) clearly dominate the upward transitions, it is interesting to notice how large the latter can also get near resonance. Here, all the rates are on picosecond timescales or less, which is a few orders of magnitude greater than in typical, femtosecond intramolecular vibrational energy redistribution [56]. This can be attributed to both the weak phonon couplings and spectral density. As the polaritons become more photonic, the rates rapidly decrease even further—something that is also explained by our definition of g_{eff} [see Eq. (5)].

The slight asymmetry around resonance is much more pronounced in Fig. 2(c), especially with the dephasing of LP. While this rate remains below nanosecond timescales at smaller cavity thicknesses, it rapidly vanishes at larger thicknesses equally far from the resonance. We attribute this behavior to the asymmetric dependence $E_c \propto 1/L_c$. Still, because the other dephasing channels operate on attosecond timescales, we can omit coherences in the following section and focus on the incoherent quantum jumps.

The polaritonic (R)ISC rates in Fig. 2(d) are particularly small, which is explained by their inverse scaling with N . Note also that even though the RISC rate $\Gamma_{T_n \rightarrow P_-}$ (pink, dashed) can exceed the ISC rate $\Gamma_{P_- \rightarrow T_n}$ (red, solid), the *total* RISC rate (sum of dashed curves) always remains below the *total* ISC rate (sum of solid curves). But if the polariton branch depopulates fast enough, even nonradiatively, there will be nothing left to convert into triplets. Still, Fig. 2(e) suggests that there

is no prospect of enhancing nonradiative processes. On the contrary, Fig. 2(e) illustrates the ability of polaritons to effectively decouple from phonons [34]. Once again, the asymmetry is highly noticeable.

Finally, the rates of emission shown in Fig. 2(f)— κ in the case of POLEDs and MOLEDs, $\Gamma_{S_n \rightarrow M}^{free}$ in the case of OLEDs—are independent of the cavity thickness. While the measured free-space emission rate of 3DPA3CN is $1.61 \times 10^8 \text{ s}^{-1}$ [53], the value here, $\sim 10^7 \text{ s}^{-1}$, makes perfect sense, as we are focusing on the $^*0 \leftrightarrow 0$ transition with lower oscillator strength. In the considered range of cavity thickness, the Purcell factor decreases monotonically, almost linearly, from 29 to 19. Since perfect spectral overlap is extremely challenging to achieve, Purcell factors in practical devices tend to range between 1 and 10 [57–62]. For example, the Purcell factor in Ref. [29], comparing with [53], is $F_P \approx 1.4$. Note that, in the absence of radiative pumping, also $\Gamma_{S_n \rightarrow M}^{weak}$ can be interpreted as the rate of MOLED emission. In fact, it is the smaller of κ and $\Gamma_{S_n \rightarrow M}^{weak}$ that primarily determines this process.

III. RATE EQUATIONS

The population dynamics of UP, ER, LP, and triplets can be calculated by plugging all the jump operators into Eq. (12) and simply taking the expectation values $\langle \dot{P}_+ \rangle$, $\langle \dot{D} \rangle = \sum_{k=1}^{N-1} \langle \dot{D}_k \rangle$, $\langle \dot{P}_- \rangle$, and $\langle \dot{T} \rangle = \sum_{n=1}^N \langle \dot{T}_n \rangle$, where $\langle \dot{X} \rangle = \langle X | \dot{\rho} | X \rangle$. Due to the rapid dephasing [see Fig. 2(c)], ρ is approximately diagonal in its eigenbasis, which means that the coherences and unitary dynamics can be omitted. The resulting system of coupled rate equations reads

$$\begin{aligned} \langle \dot{P}_+ \rangle &= \Gamma_{\mathcal{G} \rightarrow P_+} \langle \mathcal{G} \rangle + \Gamma_{D_k \rightarrow P_+} \langle D \rangle + \Gamma_{P_- \rightarrow P_+} \langle P_- \rangle + \Gamma_{T_n \rightarrow P_+} \langle T \rangle \\ &\quad - \left[\Gamma_{P_+ \rightarrow \mathcal{G}} + (N-1)\Gamma_{P_+ \rightarrow D_k} + \Gamma_{P_+ \rightarrow P_-} + N\Gamma_{P_+ \rightarrow T_n} + |\beta|^2 \kappa \right] \langle P_+ \rangle, \end{aligned} \quad (58)$$

$$\begin{aligned} \langle \dot{D} \rangle &= (N-1) \left[\Gamma_{\mathcal{G} \rightarrow D_k} \langle \mathcal{G} \rangle + \Gamma_{P_+ \rightarrow D_k} \langle P_+ \rangle + \Gamma_{P_- \rightarrow D_k} \langle P_- \rangle + \Gamma_{T_n \rightarrow D_k} \langle T \rangle \right] \\ &\quad - \left[\Gamma_{D_k \rightarrow \mathcal{G}} + \Gamma_{D_k \rightarrow P_+} + \Gamma_{D_k \rightarrow P_-} + N\Gamma_{D_k \rightarrow T_n} \right] \langle D \rangle, \end{aligned} \quad (59)$$

$$\begin{aligned} \langle \dot{P}_- \rangle &= \Gamma_{\mathcal{G} \rightarrow P_-} \langle \mathcal{G} \rangle + \Gamma_{P_+ \rightarrow P_-} \langle P_+ \rangle + \Gamma_{D_k \rightarrow P_-} \langle D \rangle + \Gamma_{T_n \rightarrow P_-} \langle T \rangle \\ &\quad - \left[\Gamma_{P_- \rightarrow \mathcal{G}} + \Gamma_{P_- \rightarrow P_+} + (N-1)\Gamma_{P_- \rightarrow D_k} + N\Gamma_{P_- \rightarrow T_n} + |\alpha|^2 \kappa \right] \langle P_- \rangle, \end{aligned} \quad (60)$$

$$\begin{aligned} \langle \dot{T} \rangle &= N \left[\Gamma_{\mathcal{G} \rightarrow T_n} \langle \mathcal{G} \rangle + \Gamma_{P_+ \rightarrow T_n} \langle P_+ \rangle + \Gamma_{D_k \rightarrow T_n} \langle D \rangle + \Gamma_{P_- \rightarrow T_n} \langle P_- \rangle \right] \\ &\quad - \left[\Gamma_{T_n \rightarrow \mathcal{G}} + \Gamma_{T_n \rightarrow P_+} + (N-1)\Gamma_{T_n \rightarrow D_k} + \Gamma_{T_n \rightarrow P_-} \right] \langle T \rangle, \end{aligned} \quad (61)$$

$$\begin{aligned} \langle \dot{\mathcal{G}} \rangle &= (\Gamma_{P_+ \rightarrow \mathcal{G}} + |\beta|^2 \kappa) \langle P_+ \rangle + \Gamma_{D_k \rightarrow \mathcal{G}} \langle D \rangle + (\Gamma_{P_- \rightarrow \mathcal{G}} + |\alpha|^2 \kappa) \langle P_- \rangle + \Gamma_{T_n \rightarrow \mathcal{G}} \langle T \rangle \\ &\quad - \left[\Gamma_{\mathcal{G} \rightarrow P_+} + (N-1)\Gamma_{\mathcal{G} \rightarrow D_k} + \Gamma_{\mathcal{G} \rightarrow P_-} + N\Gamma_{\mathcal{G} \rightarrow T_n} \right] \langle \mathcal{G} \rangle. \end{aligned} \quad (62)$$

These equations provide a comprehensive description of

POLED dynamics.

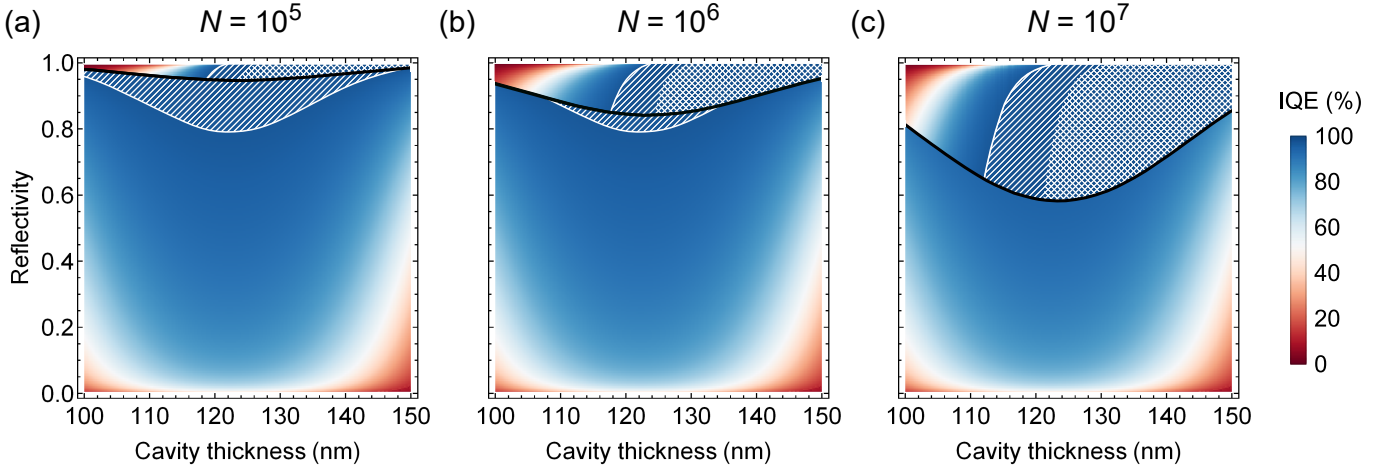


FIG. 3. Internal quantum efficiencies (IQEs) at normal incidence, as functions of cavity thickness and reflectivity, shown for different numbers of molecules. The black solid curves separate the weak-coupling regimes (below) from the strong-coupling regimes (above). In the diagonally hashed regions, MOLEDs and POLEDs beat the IQE of basic OLEDs, $\sim 97.4\%$. In the crosshatched regions, POLEDs beat both OLEDs and MOLEDs in IQE.

The operating region of MOLEDs, i.e., the weak-coupling regime, is reached with less molecules, thicker cavities, or lower reflectivities. Here, UP becomes the “missing” $k = N$ dark state that is entirely excitonic and LP becomes the Fock state $|1\rangle$. In this regime, the light-matter coupling can be treated as a perturbation, and we take interest in the singlet population that satisfies $\langle S \rangle \approx N \langle P_+ (g_{\text{eff}} = 0) \rangle \approx N \langle D (g_{\text{eff}} = 0) \rangle / (N - 1)$. The singlets, triplets, and photonic mode, which we now denote by M , are coupled via

$$\langle \dot{S} \rangle \approx N (\Gamma_{\mathcal{G} \rightarrow D_k} \langle \mathcal{G} \rangle + \Gamma_{T_n \rightarrow D_k} \langle T \rangle) - (\Gamma_{D_k \rightarrow \mathcal{G}} + \Gamma_{S_n \rightarrow M}^{\text{free}} + N \Gamma_{D_k \rightarrow T_n}) \langle S \rangle, \quad (63)$$

$$\langle \dot{M} \rangle \approx \Gamma_{S_n \rightarrow M}^{\text{weak}} \langle S \rangle - \kappa \langle M \rangle, \quad (64)$$

$$\langle \dot{T} \rangle \approx N (\Gamma_{\mathcal{G} \rightarrow T_n} \langle \mathcal{G} \rangle + \Gamma_{D_k \rightarrow T_n} \langle S \rangle) - (\Gamma_{T_n \rightarrow \mathcal{G}} + N \Gamma_{T_n \rightarrow D_k}) \langle T \rangle, \quad (65)$$

$$\langle \dot{\mathcal{G}} \rangle \approx \Gamma_{D_k \rightarrow \mathcal{G}} \langle S \rangle + \Gamma_{T_n \rightarrow \mathcal{G}} \langle T \rangle + \kappa \langle M \rangle - N (\Gamma_{\mathcal{G} \rightarrow D_k} + \Gamma_{\mathcal{G} \rightarrow T_n}) \langle \mathcal{G} \rangle. \quad (66)$$

Going to basic OLEDs, we set $R = 0$ so that $Q = 0$ and $\kappa \rightarrow \infty$. Physically, this means that the photonic mode M immediately depopulates, i.e., it gets adiabatically eliminated. The population dynamics is then given by the above equations with $\Gamma_{S_n \rightarrow M}^{\text{free}}$ replacing $\Gamma_{S_n \rightarrow M}^{\text{weak}}$ and $\kappa \langle M \rangle = \Gamma_{S_n \rightarrow M}^{\text{free}} \langle S \rangle$.

IV. INTERNAL QUANTUM EFFICIENCIES

We can now turn our attention to the figure of merit of this work, IQE, which can be expressed as

$$\text{IQE}_P = \frac{\kappa (|\beta|^2 \langle P_+ \rangle + |\alpha|^2 \langle P_- \rangle)}{\sum_X \Gamma_{\mathcal{G} \rightarrow X} \langle \mathcal{G} \rangle} \text{ for POLEDs,} \quad (67)$$

$$\text{IQE}_M = \frac{\kappa \langle M \rangle}{\sum_X \Gamma_{\mathcal{G} \rightarrow X} \langle \mathcal{G} \rangle} \text{ for MOLEDs, and} \quad (68)$$

$$\text{IQE}_O = \frac{\Gamma_{S_n \rightarrow M}^{\text{free}} \langle S \rangle}{\sum_X \Gamma_{\mathcal{G} \rightarrow X} \langle \mathcal{G} \rangle} \text{ for basic OLEDs.} \quad (69)$$

For simplicity, we omit frequency-dependent efficiency factors and angle dispersion. We evaluate the IQEs by numerically solving the rate equations (58)–(66) and substituting the steady-state populations into Eqs. (67)–(69). Again, we use the parameters in Table I and assume uniform pumping, i.e., all the molecular sites lie within the exciton formation zone. Fig. 3 shows the resulting IQEs in all coupling regimes as functions of both the cavity thickness L_c and mirror reflectivity R . The white thick curves give the IQE of basic OLEDs, $\sim 97.4\%$, while the black thick curves separate the weak-coupling regimes (MOLEDs, below) from the strong-coupling regimes (POLEDs, above). In the diagonally hashed regions, we have $\text{IQE}_{P/M} > \text{IQE}_O$. In the crosshatched regions, we have $\text{IQE}_P > \max\{\text{IQE}_M\}$.

We consider three different numbers of coupled molecules, $N = 10^5$ – 10^7 , a range that aligns with prior studies [29, 63–65]. As expected, when we go from $N = 10^5$ [Fig. 3(a)] to $N = 10^7$ [Fig. 3(c)], the strong-coupling regime expands, its border following the Gaussian shape determined by Eq. (5). Notice the trade-off involving the diagonally hashed region of MOLED advantage: for $N = 10^7$ this advantage disappears entirely. For $N = 10^8$, a third region would appear in the IQE maps, the ultrastrong-coupling regime. In all cases, the maximum IQE of MOLEDs and POLEDs is approximately 2% higher than that of the basic OLED.

The borders of the diagonally hashed MOLED advantage regions also exhibit a Gaussian shape. Hence, it is interesting to notice how drastically the corresponding borders of POLED advantage differ. In fact, they seem

to follow the Hopfield coefficient $|\alpha|^2$ [cf. Fig. 2(a)]. The more excitonic (photonic) the UP (LP) is, the better. A more excitonic UP efficiently exchanges energy with the ER, enabling effective population transfer to the LP. Conversely, if the UP is more photonic, it decouples from the ER, reducing the flow of population and limiting the system's overall efficiency. Meanwhile, a more photonic LP is advantageous as it enhances radiative decay and light extraction.

In general, the IQEs in Fig. 3 are very high. This is because, even though the ISC-RISC cycle is dominated by ISC [see Fig. 2(d)], the RISC channels outweigh the non-radiative triplet losses [see Fig. 2(e)]. In other words, it is more likely for a triplet exciton to undergo consecutive RISC and radiative relaxation than it is for a singlet exciton to undergo consecutive ISC and nonradiative relaxation. At higher singlet energies, the RISC rates become smaller and we get the conventional $\text{IQE}_{P/M/O} = 25\%$. Unaligned TDMs, greater phonon couplings, nonuniform pumping, other transition energies, and other in-plane momenta might also reduce the IQE. Nevertheless, the different coupling regions in Fig. 3 should be comparable with each other.

Importantly, IQE sets the upper bound for external quantum efficiency (EQE), because not all generated photons are extracted as usable light; some are lost due to mirror attenuation, scattering or absorption in different layers, and surface plasmon polariton (SPP) losses at interfaces [66]. Achieving $\text{EQE} = \text{IQE}$ requires minimizing these losses. One solution would be to integrate distributed Bragg reflectors, which reflect light toward the desired direction while reducing attenuation and SPP coupling [11, 67]. Additionally, optimizing the refractive indices of layers and using low-loss materials could further bridge the gap between EQE and IQE. Here, however, we focused on introducing the first unified model of OLEDs, MOLEDs, and POLEDs, laying the foundation for future EQE studies.

V. CONCLUSIONS AND DISCUSSION

In this work, we introduced the first unified quantum master equation model for OLEDs, MOLEDs, and POLEDs. Specifically, we derived the rates for electrical excitation, polariton transitions, dephasing, ISC, RISC, emission, and nonradiative losses in the weak-pumping and weak system-environment coupling regimes. Furthermore, we solved the population dynamics by incorporating these rates, along with the corresponding jump operators, into the GKSL master equation. We ap-

plied our model to calculate and compare the IQE of 3DPA3CN in all the coupling regimes. Notably, we observed that POLEDs converted excitons to photons most efficiently. While the model is relatively simple, we believe it can serve as a guide for actual device design. Importantly, evenly propagating errors would ensure that the IQEs in Fig. 3 remain comparable, meaning that $\max\{\text{IQE}_P\} > \max\{\text{IQE}_M\} > \text{IQE}_O$. While the experimental validation is beyond the scope of this work, our predictions for the trends of MOLED IQE are consistent with prior studies [19].

Expanding the model is as important as it is challenging. While we leave this task for future studies, here we speculate on how such a model might be constructed. First, a more realistic model would include all relevant transition energies, their internal conversions, and other emission angles. Second, stronger phonon couplings should be considered, introducing additional channels such as radiative pumping [68]. Non-Markovian memory effects would also become significant in this context [69, 70]. Third, achieving higher luminances—and eventually efficiency roll-off—would require stronger pumping rates and moving beyond the linear regime. Most notably, annihilation processes involving singlets, triplets, and polarons would become critical [14]. However, diagonalizing the HTC Hamiltonian in the strong-coupling regime quickly becomes a formidable task as the number of excitations grows, necessitating the use of permutation symmetries [71], mean-field approximations [72], or hierarchical equations of motion [73]. Finally, as the IQE represents the upper bound of EQE—an end-user-relevant quantity—future theoretical investigations should also address outcoupling efficiency. For example, our model could be combined with transfer matrix methods to explore this aspect [74].

ACKNOWLEDGMENTS

O.S. acknowledges fruitful discussions with A. Dutta and T. Leppälä. This project was funded by the European Research Council through the European Union's Horizon 2020 research and innovation program (Grant Agreement Number 948260) and partially by the European Innovation Council through the SCOLED project (Grant Agreement Number 101098813). Views and opinions expressed are, however, those of the authors only and do not necessarily reflect those of the European Union or the European Innovation Council. Neither the European Union nor the granting authority can be held responsible for them.

[1] S. R. Forrest, The path to ubiquitous and low-cost organic electronic appliances on plastic, *Nature* **428**, 911 (2004).

[2] C.-C. Li, H.-Y. Tseng, H.-C. Liao, H.-M. Chen, T. Hsieh, S.-A. Lin, H.-C. Jau, Y.-C. Wu, Y.-L. Hsu, W.-H. Hsu, and T.-H. Lin, Enhanced image quality of OLED trans-

- parent display by cholesteric liquid crystal back-panel, *Optics Express* **25**, 29199 (2017).
- [3] S. R. Forrest, *Organic Electronics: Foundations to Applications* (Oxford University Press, Oxford, 2020).
 - [4] Y. Huang, E.-L. Hsiang, M.-Y. Deng, and S.-T. Wu, Mini-LED, Micro-LED and OLED displays: present status and future perspectives, *Light: Science & Applications* **9**, 105 (2020).
 - [5] H. Zhu, E.-S. Shin, A. Liu, D. Ji, Y. Xu, and Y.-Y. Noh, Printable Semiconductors for Backplane TFTs of Flexible OLED Displays, *Advanced Functional Materials* **30**, 1904588 (2020).
 - [6] G. Hong, X. Gan, C. Leonhardt, Z. Zhang, J. Seibert, J. M. Busch, and S. Bräse, A Brief History of OLEDs—Emitter Development and Industry Milestones, *Advanced Materials* **33**, 2005630 (2021).
 - [7] Z.-Y. Chen, D. Yin, and J. Feng, Materials, structures, and strategies for foldable electroluminescent devices, *Advanced Optical Materials* **11**, 2300282 (2023).
 - [8] D. Volz, M. Wallesch, C. Fléchon, M. Danz, A. Verma, J. Navarro, Z. Daniel, S. Bräse, and T. Baumann, ChemInform Abstract: From Iridium and Platinum to Copper and Carbon: New Avenues for More Sustainability in Organic Light-Emitting Diodes, *Green Chemistry* **46** (2015).
 - [9] M. Franz and F. Wenzl, Critical Review on Life Cycle Inventories and Environmental Assessments of LED-Lamps, *Critical Reviews in Environmental Science and Technology* **47** (2017).
 - [10] N. Schulte-Römer, J. Meier, M. Söding, and E. Danneemann, The LED Paradox: How Light Pollution Challenges Experts to Reconsider Sustainable Lighting, *Sustainability* **11** (2019).
 - [11] E. Palo and K. S. Daskalakis, Prospects in Broadening the Application of Planar Solution-Based Distributed Bragg Reflectors, *Advanced Materials Interfaces* **10**, 2202206 (2023).
 - [12] H. Yersin, A. F. Rausch, R. Czerwieniec, T. Hofbeck, and T. Fischer, The triplet state of organo-transition metal compounds. Triplet harvesting and singlet harvesting for efficient OLEDs, *Coordination Chemistry Reviews* **255**, 2622 (2011).
 - [13] N. C. Giebink and S. R. Forrest, Quantum efficiency roll-off at high brightness in fluorescent and phosphorescent organic light emitting diodes, *Physical Review B* **77**, 235215 (2008).
 - [14] C. Murawski, K. Leo, and M. C. Gather, Efficiency roll-off in organic light-emitting diodes, *Advanced Materials* **25**, 6801 (2013).
 - [15] S. Diesing, L. Zhang, E. Zysman-Colman, and I. D. W. Samuel, A figure of merit for efficiency roll-off in TADF-based organic LEDs, *Nature* **627**, 747 (2024).
 - [16] E. Tankelevičiūtė, I. D. Samuel, and E. Zysman-Colman, The Blue Problem: OLED Stability and Degradation Mechanisms, *Journal of Physical Chemistry Letters* **15**, 1034 (2024).
 - [17] S. Dirr, S. Wiese, H.-H. Johannes, and W. Kowalsky, Organic Electro- and Photoluminescent Microcavity Devices, *Advanced Materials* **10**, 167 (1998).
 - [18] C. Xiang, W. Koo, F. So, H. Sasabe, and J. Kido, A systematic study on efficiency enhancements in phosphorescent green, red and blue microcavity organic light emitting devices, *Light: Science & Applications* **2**, e74 (2013).
 - [19] C. Murawski, P. Liehm, K. Leo, and M. C. Gather, Influence of Cavity Thickness and Emitter Orientation on the Efficiency Roll-Off of Phosphorescent Organic Light-Emitting Diodes, *Advanced Functional Materials* **24**, 1117 (2014).
 - [20] C. Ye, S. Mallick, M. Hertzog, M. Kowalewski, and K. Börjesson, Direct Transition from Triplet Excitons to Hybrid Light-Matter States via Triplet-Triplet Annihilation, *Journal of the American Chemical Society* **143**, 7501 (2021).
 - [21] H. Zhao, C. E. Arneson, D. Fan, and S. R. Forrest, Stable blue phosphorescent organic LEDs that use polariton-enhanced Purcell effects, *Nature* **626**, 300 (2024).
 - [22] K. Vahala, Optical microcavities, *Nature* **424**, 839 (2003).
 - [23] R. Bhuyan, J. Mony, O. Kotov, G. W. Castellanos, J. Gómez Rivas, T. O. Shegai, and K. Börjesson, The Rise and Current Status of Polaritonic Photochemistry and Photophysics, *Chemical Reviews* **123**, 10877 (2023).
 - [24] A. Mischok, S. Hillebrandt, S. Kwon, and M. C. Gather, Highly efficient polaritonic light-emitting diodes with angle-independent narrowband emission, *Nature Photonics* **17**, 393 (2023).
 - [25] A. G. Abdelmagid, H. A. Qureshi, M. A. Papachatzakis, O. Siltanen, M. Kumar, A. Ashokan, S. Salman, K. Luoma, and K. S. Daskalakis, Identifying the origin of delayed electroluminescence in a polariton organic light-emitting diode, *Nanophotonics* **13**, 2565 (2024).
 - [26] S. Yuan, Y. Guan, Y. Zhao, C. An, B. Liao, C. Gu, Z. Sun, Q. Liao, and H. Fu, Colorful Narrow-Band Organic Polariton Light-emitting Diodes Based on a Single Emitter, *Laser & Photonics Reviews* **n/a**, 2401532 (2024).
 - [27] G. Sandik, J. Feist, F. J. García-Vidal, and T. Schwartz, Cavity-enhanced energy transport in molecular systems, *Nature Materials* **n/a**, 1 (2024).
 - [28] K. Stranius, M. Hertzog, and K. Börjesson, Selective manipulation of electronically excited states through strong light-matter interactions, *Nature Communications* **9**, 2273 (2018).
 - [29] E. Eizner, L. A. Martínez-Martínez, J. Yuen-Zhou, and S. Kéna-Cohen, Inverting singlet and triplet excited states using strong light-matter coupling, *Science Advances* **5**, eaax4482 (2019).
 - [30] Y. Yu, S. Mallick, M. Wang, and K. Börjesson, Barrier-free reverse-intersystem crossing in organic molecules by strong light-matter coupling, *Nature Communications* **12**, 1 (2021).
 - [31] O. Siltanen, K. Luoma, A. J. Musser, and K. S. Daskalakis, Enhancing the efficiency of polariton OLEDs in and beyond the single-excitation subspace (2024), arXiv:2404.04257 [cond-mat.mtrl-sci].
 - [32] P. Rebentrost, M. Mohseni, and A. Aspuru-Guzik, Role of Quantum Coherence and Environmental Fluctuations in Chromophoric Energy Transport, *The Journal of Physical Chemistry B* **113**, 9942 (2009).
 - [33] M. Nakano, S. Ito, T. Nagami, Y. Kitagawa, and T. Kubo, Quantum Master Equation Approach to Singlet Fission Dynamics of Realistic/Artificial Pentacene Dimer Models: Relative Relaxation Factor Analysis, *The Journal of Physical Chemistry C* **120**, 22803 (2016).
 - [34] F. Herrera and F. C. Spano, Absorption and photoluminescence in organic cavity QED, *Physical Review A* **95**, 053867 (2017).
 - [35] S. Takahashi, K. Watanabe, and Y. Matsumoto, Singlet

- fission of amorphous rubrene modulated by polariton formation, *The Journal of Chemical Physics* **151**, 074703 (2019).
- [36] L. A. Martínez-Martínez, E. Eizner, S. Kéna-Cohen, and J. Yuen-Zhou, Triplet harvesting in the polaritonic regime: A variational polaron approach, *Journal of Chemical Physics* **151**, 054106 (2019).
- [37] B. Gu and S. Mukamel, Optical-Cavity Manipulation of Conical Intersections and Singlet Fission in Pentacene Dimers, *The Journal of Physical Chemistry Letters* **12**, 2052 (2021).
- [38] A. Carreras and D. Casanova, Theory of Exciton Dynamics in Thermally Activated Delayed Fluorescence, *ChemPhotoChem* **6**, e202200066 (2022).
- [39] E. Fermi, *Nuclear Physics* (University of Chicago Press, Chicago, 1950).
- [40] R. A. Marcus, On the Theory of Oxidation-Reduction Reactions Involving Electron Transfer. I, *The Journal of Chemical Physics* **24**, 966 (1956).
- [41] H.-P. Breuer and F. Petruccione, *The Theory of Open Quantum Systems* (Oxford University Press, Oxford, 2007).
- [42] N. Lydick, J. Hu, and H. Deng, Dimensional dependence of a molecular-polariton mode number, *Journal of the Optical Society of America B* **41**, C247 (2024).
- [43] S. Richter, T. Michalsky, L. Fricke, C. Sturm, H. Franke, M. Grundmann, and R. Schmidt-Grund, Maxwell consideration of polaritonic quasi-particle Hamiltonians in multi-level systems, *Applied Physics Letters* **107**, 231104 (2015).
- [44] C. Majenz, T. Albash, H.-P. Breuer, and D. A. Lidar, Coarse graining can beat the rotating-wave approximation in quantum Markovian master equations, *Physical Review A* **88**, 012103 (2013).
- [45] Y. Wang and J. Y. Haw, Bridging the gap between the Jaynes-Cummings and Rabi models using an intermediate rotating wave approximation, *Physics Letters A* **379**, 779 (2015).
- [46] Y. Sang, C.-Y. Wang, S. S. Raja, C.-W. Cheng, C.-T. Huang, C.-A. Chen, X.-Q. Zhang, H. Ahn, C. Shih, Y.-H. Lee, J. Shi, and S. Gwo, Tuning of Two-Dimensional Plasmon-Exciton Coupling in Full Parameter Space: A Polaritonic Non-Hermitian System, *Nano Letters* **21**, 2596 (2021).
- [47] B. Kratochwil, J. V. Koski, A. J. Landig, P. Scarlino, J. C. Abadillo-Uriel, C. Reichl, S. N. Coppersmith, W. Wegscheider, M. Friesen, A. Wallraff, T. Ihn, and K. Ensslin, Charge qubit in a triple quantum dot with tunable coherence, *Physical Review Research* **3**, 013171 (2021).
- [48] C. Lin, P. Han, S. Xiao, F. Qu, J. Yao, X. Qiao, D. Yang, Y. Dai, Q. Sun, D. Hu, A. Qin, Y. Ma, B. Z. Tang, and D. Ma, Efficiency Breakthrough of Fluorescence OLEDs by the Strategic Management of “Hot Excitons” at Highly Lying Excitation Triplet Energy Levels, *Advanced Functional Materials* **31**, 1 (2021).
- [49] K. O. Cheon and J. Shinar, Electroluminescence spikes, turn-off dynamics, and charge traps in organic light-emitting devices, *Physical Review B* **69**, 201306 (2004).
- [50] T. D. Barrett, T. H. Doherty, and A. Kuhn, Pushing Purcell enhancement beyond its limits, *New Journal of Physics* **22**, 063013 (2020).
- [51] R. K. Pathria and P. D. Beale, *Statistical mechanics* (Elsevier, Amsterdam, 2011).
- [52] P. Forn-Díaz, L. Lamata, E. Rico, J. Kono, and E. Solano, Ultrastrong coupling regimes of light-matter interaction, *Reviews of Modern Physics* **91**, 025005 (2019).
- [53] M. Taneda, K. Shizu, H. Tanaka, and C. Adachi, High efficiency thermally activated delayed fluorescence based on 1,3,5-tris(4-(diphenylamino)phenyl)-2,4,6-tricyanobenzene, *Chemical Communications* **51**, 5028 (2015).
- [54] A. Dutta, V. Tiainen, and J. J. Toppari, Optimizing geometry of low-Q all-metal Fabry-Pérot microcavity for fluorescence spectroscopy, *IOP SciNotes* **2**, 015205 (2021).
- [55] C. Gerry and P. Knight, *Introductory Quantum Optics* (Cambridge University Press, Cambridge, 2004).
- [56] D. G. Lidzey, A. M. Fox, M. D. Rahn, M. S. Skolnick, V. M. Agranovich, and S. Walker, Experimental study of light emission from strongly coupled organic semiconductor microcavities following nonresonant laser excitation, *Physical Review B* **65**, 195312 (2002).
- [57] A. Dodabalapur, L. J. Rothberg, R. H. Jordan, T. M. Miller, R. E. Slusher, and J. M. Phillips, Physics and applications of organic microcavity light emitting diodes, *Journal of Applied Physics* **80**, 6954 (1996).
- [58] J. Blondelle, H. De Neve, G. Borghs, P. Daele, P. Demeester, and R. Baets, High efficiency (>20%) microcavity LEDs, in *Semiconductor Optical Microcavity Devices and Photonic Bandgaps*, Vol. 5 (1997) pp. 1–6.
- [59] V. Bulović, V. B. Khalfin, G. Gu, P. E. Burrows, D. Z. Garbuzov, and S. R. Forrest, Weak microcavity effects in organic light-emitting devices, *Physical Review B* **58**, 3730 (1998).
- [60] D. Delbeke, R. Bockstaele, P. Bienstman, R. Baets, and H. Benisty, High-efficiency semiconductor resonant-cavity light-emitting diodes: a review, *IEEE Journal of Selected Topics in Quantum Electronics* **8**, 189 (2002).
- [61] A. Genco, G. Giordano, S. Carallo, G. Accorsi, Y. Duan, S. Gambino, and M. Mazzeo, High quality factor microcavity OLED employing metal-free electrically active Bragg mirrors, *Organic Electronics* **62**, 174 (2018).
- [62] J. Kaupp, Y. Reum, F. Kohr, J. Michl, Q. Buchinger, A. Wolf, G. Peniakov, T. Huber-Loyola, A. Pfenning, and S. Höfling, Purcell-Enhanced Single-Photon Emission in the Telecom C-Band, *Advanced Quantum Technologies* **6**, 2300242 (2023).
- [63] T. Schwartz, J. A. Hutchison, J. Léonard, C. Genet, S. Haacke, and T. W. Ebbesen, Polariton Dynamics under Strong Light-Molecule Coupling, *ChemPhysChem* **14**, 125 (2013).
- [64] R. Pandya, R. Y. S. Chen, Q. Gu, J. Sung, C. Schneidermann, O. S. Ojambati, R. Chikkaraddy, J. Gorman, G. Jacucci, O. D. Onelli, T. Willhammar, D. N. Johnstone, S. M. Collins, P. A. Midgley, F. Auras, T. Baikie, R. Jayaprakash, F. Mathevet, R. Soucek, M. Du, A. M. Alvertis, A. Ashoka, S. Vignolini, D. G. Lidzey, J. J. Baumberg, R. H. Friend, T. Barisien, L. Legrand, A. W. Chin, J. Yuen-Zhou, S. K. Saikin, P. Kukura, A. J. Musser, and A. Rao, Microcavity-like exciton-polaritons can be the primary photoexcitation in bare organic semiconductors, *Nature Communications* **12**, 6519 (2021).
- [65] Q. Ou, Y. Shao, and Z. Shuai, Enhanced Reverse Intersystem Crossing Promoted by Triplet Exciton-Photon Coupling, *Journal of the American Chemical Society* **143**, 17786 (2021).

- [66] R. Shinar and J. Shinar, Light extraction from organic light emitting diodes (OLEDs), *Journal of Physics: Photonics* **4**, 032002 (2022).
- [67] W. He, Q. Sun, Z.-Y. Jin, H.-F. Zheng, S.-Q. Sun, J.-G. Zhou, S.-C. Hou, Y.-M. Xie, F. Kang, G. Wei, and M.-K. Fung, Narrowband emission and enhanced stability in top-emitting OLEDs with dual resonant cavities, *Materials Horizons* , (2025).
- [68] J. B. Pérez-Sánchez and J. Yuen-Zhou, Radiative pumping vs vibrational relaxation of molecular polaritons: a bosonic mapping approach (2024), arXiv:2407.20594 [quant-ph].
- [69] H.-P. Breuer, E.-M. Laine, J. Piilo, and B. Vacchini, Colloquium: Non-Markovian dynamics in open quantum systems, *Reviews of Modern Physics* **88**, 021002 (2016).
- [70] I. de Vega and D. Alonso, Dynamics of non-Markovian open quantum systems, *Reviews of Modern Physics* **89**, 015001 (2017).
- [71] J. A. Campos-Gonzalez-Angulo and J. Yuen-Zhou, Generalization of the Tavis-Cummings model for multi-level anharmonic systems: Insights on the second excitation manifold, *The Journal of Chemical Physics* **156**, 194308 (2022).
- [72] H. Hu, H. Deng, and X.-J. Liu, Polariton-polariton interaction beyond the Born approximation: A toy model study, *Physical Review A* **102**, 063305 (2020).
- [73] Y. Tanimura, Numerically "exact" approach to open quantum dynamics: The hierarchical equations of motion (HEOM), *The Journal of Chemical Physics* **153**, 020901 (2020).
- [74] B. C. Krummacher, S. Nowy, J. Frischeisen, M. Klein, and W. Brütting, Efficiency analysis of organic light-emitting diodes based on optical simulation, *Organic Electronics* **10**, 478 (2009).